What is the neutral wind in height-integrated ionospheric electrodynamics?

S. M. Hatch[1], J. K. Burchill[2], H. Vanhamäki[3], R. L. A. Mesquita[4], K. M. Laundal[1], D. J. Knudsen[2]

[1]Department of Physics and Technology, University of Bergen, Bergen, Norway
[2]Department of Physics and Astronomy, University of Calgary, Calgary, Alberta, Canada
[3]Space Physics and Astronomy Research Unit, University of Oulu, Oulu, Finland
[4]Johns Hopkins University Applied Physics Laboratory, Laurel, MD, USA

Key Points:

- There is generally no single suitable definition of the neutral wind in height-integrated descriptions of ionosphere-thermosphere dynamics
- The expression $\Sigma_P|\mathbf{E}+\mathbf{U}\times\mathbf{B}|^2$ for height-integrated Joule heating is strictly a lower bound
- The errors that E-region wind shears introduce in common expressions for key IT parameters increase with increasing geomagnetic activity

Corresponding author: Spencer Mark Hatch, `spencer.hatch@uib.no`

Abstract

In most large-scale MHD models of Earth's space environment, coupling between the magnetosphere and the ionosphere-thermosphere (IT) is addressed by representing the latter as a two-dimensional spherical shell. Similarly, most empirical models of IT electrodynamics are based on solving the height-integrated ionospheric Ohm's law on a spherical shell. We show that there is in general no single suitable definition of the neutral wind term in high-latitude, height-integrated IT electrodynamics. Instead, two neutral wind terms weighted by Hall and Pedersen conductivities appear. We show that a commonly used expression for Joule heating in terms of height-integrated quantities is a lower bound of the actual Joule heating. Using neutral wind profiles derived from sounding rocket chemical release experiments near Poker Flat, Alaska, and Poker Flat Incoherent Scatter Radar (PFISR) measurements, we find differences of order 10–100 m/s between the two neutral wind terms.

Plain Language Summary

The Earth's ionosphere at altitudes of ∼80 to a few hundred km overlaps with upper atmospheric layer known as the thermosphere. One of the largest challenges facing researchers who are trying to understand how these regions are connected is the fact that it is difficult to make measurements of the atmospheric winds at these altitudes. This is a problem because these winds can vary drastically with altitude. In this study we demonstrate how such variations can make it impossible to faithfully represent the 3D atmospheric winds with a single 2D vector field in 2D representations of ionospheric electrodynamics, and how 2D representations underestimate the atmospheric heating that is caused by friction between charged and neutral particles. We then use radar measurements and rocket-measured altitude profiles of atmospheric winds to estimate how large the errors associated with 2D representations of ionospheric electrodynamics can be.

1 Introduction

Earth's overlapping ionosphere-thermosphere (IT) region is the site of mechanical and electrodynamic coupling between the neutral atmosphere and plasmas of both terrestrial (magnetospheric and ionospheric) and extraterrestrial (solar wind) origin. Much of the electrodynamics within this region can be described in terms of a three-fluid model consisting of neutral, ion, and electron fluids in the presence of a strong background magnetic field (Section 9.5 in Parker, 2007).

A common point of reference for a vast number of experimental investigations of high-latitude IT electrodynamics is the horizontal component of the ionospheric Ohm's law assuming steady-state stress balance between Lorentz and collisional drag forces and neglecting all other forces in the ion momentum equation (Section 5 in Chapman, 1956):

$$\mathbf{j}_\perp = \sigma_P \left(\mathbf{E}_\perp + \mathbf{u} \times \mathbf{B}\right) + \sigma_H \mathbf{b} \times \left(\mathbf{E}_\perp + \mathbf{u} \times \mathbf{B}\right), \tag{1}$$

with σ_P and σ_H Pedersen and Hall conductivities, and $\mathbf{E}_\perp$, $\mathbf{B}$, and $\mathbf{u}$ the ionospheric electric field, the total (background plus perturbation) magnetic field, and the neutral wind. The corresponding Joule heating density (heat transfer rate per volume) is given by

$$w_J = \mathbf{j}_\perp \cdot \left(\mathbf{E}_\perp + \mathbf{u} \times \mathbf{B}\right) = \sigma_P |\left(\mathbf{E}_\perp + \mathbf{u} \times \mathbf{B}\right)|^2. \tag{2}$$

Both $\mathbf{j}_\perp$ and w_J are independent of reference frame in (magnetic) Galilean relativity (Mannucci et al., 2022) by virtue of the fact that they are defined in terms of the sum of the electric field and the "neutral wind dynamo" $\mathbf{u} \times \mathbf{B}$.

One experimental investigation of Equations 1 and 2 was the Joule II suborbital sounding rocket campaign. Using in situ measurements of electric field, bulk ion drift, and neutral wind in the vicinity of a relatively quiescent auroral breakup in northern Alaska, Sangalli et al. (2009) reported the errors in E-region ion-neutral momentum transfer collision frequency and Joule heating altitude profiles that would arise if the neutral winds were assumed to be zero. In a separate analysis of these and additional rocket and ground-based observations from the same campaign, Burchill et al. (2012) found evidence for horizontal or vertical structuring in ion-neutral collision frequencies on scales of 1–10 km.

Such comprehensive altitude profiles are rare, and instead one frequently encounters a height-integrated form of the ionospheric Ohm's law:

$$\mathbf{J}_\perp = \Sigma_P \left(\mathbf{E}_\perp + \mathbf{U} \times \mathbf{B}\right) + \Sigma_H \mathbf{b} \times \left(\mathbf{E}_\perp + \mathbf{U} \times \mathbf{B}\right), \tag{3}$$

where Σ_P and Σ_H are the Pedersen and Hall conductances (conductivities integrated over altitude). This form is obtained by integrating Equation 2 over altitude assuming that $\mathbf{B}$ is radial, that $\mathbf{B}$ and $\mathbf{E}_\perp$ are independent of altitude over ionospheric E- and F-region altitudes ($\sim$100–250 km), and that $\mathbf{U}$ is the height-averaged neutral wind or a "representative" or "effective" neutral wind at a particular altitude. (The neutral wind $\mathbf{U}$ in particular is often assumed to be zero in Earth's rotating frame of reference. A brief summary of the implications of assuming the E-field is constant with altitude is given in Text S1 of the Supporting Information.) With these assumptions one may define a height-integrated Joule heating rate

$$W_J = \int w_J \, dh = \mathbf{J}_\perp \cdot \left(\mathbf{E}_\perp + \mathbf{U} \times \mathbf{B}\right) = \Sigma_P \left(\mathbf{E}_\perp + \mathbf{U} \times \mathbf{B}\right)^2, \tag{4}$$

and estimate ionospheric conductances via the expressions

$$\Sigma_H = \pm\hat{\mathbf{r}} \cdot \left[\mathbf{J}_\perp \times \left(\mathbf{E}_\perp + \mathbf{U} \times \mathbf{B}\right)\right] / |\mathbf{E}_\perp + \mathbf{U} \times \mathbf{B}|^2; \tag{5}$$

$$\Sigma_P = \mathbf{J}_\perp \cdot \left(\mathbf{E}_\perp + \mathbf{U} \times \mathbf{B}\right) / |\mathbf{E}_\perp + \mathbf{U} \times \mathbf{B}|^2; \tag{6}$$

where the upper and lower signs of the RHS in Equation 5 are respectively for the Northern and Southern Hemisphere. The approach represented by Equation 4 to estimating height-integrated Joule heating dates at least back to the work of Cole (1975) and continues to be used widely, while the approach to estimating conductances represented by Equations 5–6 originates with Amm (2001). This approach has been used by a number of studies over the past two decades, and has elsewhere been referred to as the "elementary current method" or the "electrodynamic method" (e.g., Amm, 2001; Green et al., 2007; Weimer & Edwards, 2021; Hatch et al., 2023).

The height-integrated approach to ionospheric electrodynamics represented by Equations 3–6 is oversimplified: Earth's magnetic field lines are not radial, ionospheric electric fields do not necessarily map along field lines (Farley, 1959), and the horizontal components of the neutral wind exhibit the nearly permanent presence of vertical shears over altitudes of 80 to 140 km (Heppner & Miller, 1982; Larsen, 2002; Sangalli et al., 2009). More advanced treatments of ionospheric electrodynamics that account for such complications, such as that presented by Richmond (1995), nevertheless remain unused in a large number of experimental studies and data assimilation techniques (e.g., Richmond & Kamide, 1988; Matsuo, 2020; Laundal et al., 2022) because we lack the body of robust 3D measurements of the IT system needed to make use of them (Palmroth et al., 2021). For similar reasons, in the majority of existing global MHD models the coupling between the magnetosphere and the IT system is founded on what Mannucci et al. (2022) term a "key magnetosphere-ionosphere coupling equation" derived from current continuity (their Equation 11; see also Merkin & Lyon, 2010; Mukhopadhyay et al., 2021, and references therein) in which the neutral wind is assumed to be zero or constant with altitude.

In this study, we explore some of the implications of the commonly employed assumption that the neutral wind is independent of altitude that is necessary to arrive at

Equations 3–6 and the current continuity equation used in magnetosphere-ionosphere coupling. In Section 2 we summarize central quantities and equations in a height-integrated description of IT electrodynamics when the neutral wind is not assumed to be independent of altitude. In Section 3 we present neutral wind profiles derived from rocket-borne trimethylaluminum (TMA) chemical release experiments launched from the Poker Flat Research Range (PFRR) between 2007 and 2018 together with conductivity profiles calculated from measurements made by the Poker Flat Incoherent Scatter Radar (PFISR), and use these to understand how the assessment of the local IT electrodynamics is modified by assuming the neutral wind is independent of altitude. In Section 4 we summarize our findings.

2 Defining the neutral wind in height-integrated IT electrodynamics

Relaxing the assumption that $\mathbf{u}$ does not vary with height, integration of Ohm's law (Equation 1) over ionospheric altitudes yields

$$\mathbf{J}_\perp = \Sigma_P \mathbf{F}_P + \Sigma_H \hat{\mathbf{b}} \times \mathbf{F}_H = \Sigma_P \mathbf{F}_P + \Sigma_H \hat{\mathbf{b}} \times \mathbf{F}_P + \Sigma_H \hat{\mathbf{b}} \times (\mathbf{U}_H - \mathbf{U}_P) \times \mathbf{B}, \tag{7}$$

where

$$\mathbf{F}_c = \mathbf{E}_\perp + \mathbf{U}_c \times \mathbf{B}; \tag{8}$$

$$\mathbf{U}_c = \frac{1}{\Sigma_c} \int \sigma_c \, \mathbf{u} \, dh; \tag{9}$$

and c is either H or P. The integration is performed over all ionospheric altitudes. We refer to the conductivity-weighted neutral wind terms $\mathbf{U}_H$ and $\mathbf{U}_P$ as the Hall-weighted or Pedersen-weighted neutral winds. The latter has been termed the "effective neutral wind" by Lu et al. (1995) and plays a role in estimates of height-integrated Joule heating and the Pedersen conductance, which we discuss below. The distinction between the Hall-weighted and Pedersen-weighted neutral winds disappears when the two conductivity profiles differ by no more than a constant factor, or when the neutral wind $\mathbf{u}$ does not vary with altitude. As noted in the Introduction, these idealized conditions are virtually never manifest in measured altitude profiles of the neutral winds.

Taking the dot product of Equation 7 with $\mathbf{F}_P$ yields

$$\mathbf{J}_\perp \cdot \mathbf{F}_P = \Sigma_P F_P^2 + M \, \Sigma_H, \tag{10}$$

where

$$M = B \left[\mathbf{E}_\perp \cdot (\mathbf{U}_H - \mathbf{U}_P) + \mathbf{B} \cdot (\mathbf{U}_H \times \mathbf{U}_P) \right]. \tag{11}$$

The radial component of the cross product of Equation 7 with $\mathbf{F}_H$ is

$$\hat{\mathbf{r}} \cdot (\mathbf{J}_\perp \times \mathbf{F}_H) = \pm \Sigma_H F_H^2 \pm M \, \Sigma_P, \tag{12}$$

with the upper sign for the Northern Hemisphere.

Equations 10 and 12 can be simultaneously solved to obtain generalizations of Equations 5 and 6 for height-integrated conductances in terms of the Hall-weighted and Pedersen-weighted neutral winds:

$$\Sigma_H = \frac{\pm |\mathbf{F}_P^2| \, \hat{\mathbf{r}} \cdot (\mathbf{J}_\perp \times \mathbf{F}_H) - M \, \mathbf{J}_\perp \cdot \mathbf{F}_P}{|\mathbf{F}_H^2||\mathbf{F}_P^2| - M^2}; \tag{13}$$

$$\Sigma_P = \frac{\mathbf{J}_\perp \cdot \mathbf{F}_P}{|\mathbf{F}_P|^2} \left(1 + \frac{M^2}{|\mathbf{F}_H|^2 |\mathbf{F}_P|^2 - M^2} \right) \mp M \frac{\hat{\mathbf{r}} \cdot (\mathbf{J}_\perp \times \mathbf{F}_H)}{|\mathbf{F}_H|^2 |\mathbf{F}_P|^2 - M^2}. \tag{14}$$

When $\mathbf{U}_H = \mathbf{U}_P$ we have $M = 0$, and Equations 13 and 14 reduce to the expressions for Hall and Pedersen conductances given by Equations 5 and 6.

Integrating the right-hand side of the expression for Joule heating density (2), we obtain

$$W_J = \Sigma_P \left[E_\perp^2 + 2\mathbf{E}_\perp \cdot (\mathbf{U}_P \times \mathbf{B}) \right] + \int \sigma_P \|\mathbf{u} \times \mathbf{B}\|^2 \, dh. \tag{15}$$

This expression cannot directly be brought into the more familiar form $\Sigma_P \left(\mathbf{E}_\perp + \mathbf{U} \times \mathbf{B} \right)^2$ for some appropriately chosen $\mathbf{U}$ (cf. Equation 4) because of the integral in the last term. However, one may show explicitly via the Cauchy-Bunyakovsky-Schwarz inequality that $\int \sigma_P \|\mathbf{u} \times \mathbf{B}\|^2 \, dh \geq \Sigma_P \left(\mathbf{U}_P \times \mathbf{B} \right)^2$ (see Text S2 in Supporting Information). Then the following inequalities hold:

$$\begin{aligned} W_J &\geq \Sigma_P \left(\mathbf{E}_\perp + \mathbf{U}_P \times \mathbf{B} \right)^2 = \Sigma_P \mathbf{F}_P^2; \\ \Sigma_P &\leq W_J / \mathbf{F}_P^2. \end{aligned} \tag{16}$$

Thus when the variable $\mathbf{U}$ is replaced with $\mathbf{U}_P$ in Equations 4 and 6, these equations are in fact lower and upper bounds, respectively, on the true height-integrated Joule heating and Pedersen conductance. When the neutral wind does not vary with altitude we have $\mathbf{U}_P \to \mathbf{U}$ in Inequality 16, such that the height-integrated Joule heating $W_J = \Sigma_P (\mathbf{E} + \mathbf{U} \times \mathbf{B})^2$ and the Pedersen conductance $\Sigma_P = W_J / (\mathbf{E} + \mathbf{U} \times \mathbf{B})^2$ as given by Equations 4 and 6.

From the foregoing we see that for estimation of height-integrated Joule heating and the Pedersen conductance, the Pedersen-weighted neutral wind $\mathbf{U}_P$ constitutes the most natural definition of the "effective" neutral wind, as indirectly suggested by Lu et al. (1995).

3 Experimental examination of Hall- and Pedersen-weighted neutral winds

Section 2 illustrates that it is in general not possible to uniquely define the neutral wind term in height-integrated (or for that matter field line-integrated) treatments of IT electrodynamics. Instead, the neutral wind appears as two separate terms weighted separately by the Hall and Pedersen conductivity profiles, here defined by Equation 9 and respectively denoted by $\mathbf{U}_H$ and $\mathbf{U}_P$. This situation begs the following questions:

1. How large is the observed difference between $\mathbf{U}_H$ and $\mathbf{U}_P$?
2. How much better are various rule-of-thumb approximations for the neutral wind (e.g., the suggestion from Lu et al., 1995, that the "winds at 160 km" are representative of the "effective neutral wind") than simply assuming $\mathbf{U}_H = \mathbf{U}_P = \mathbf{u} = 0$?
3. Are the differences between $\mathbf{U}_H$ and $\mathbf{U}_P$ meaningful for assessments of IT electrodynamics?

To answer these questions we use horizontal neutral wind profiles derived from TMA chemical release experiments carried by sounding rockets during five campaigns launched from the Poker Flat Research Range (Mesquita, 2021, and references therein), as well as conductivity profiles derived from Poker Flat Incoherent Scatter Radar (PFISR) measurements and empirical models of ionospheric and atmospheric composition, atmospheric temperature, and Earth's magnetic field.

3.1 Measurements and models

Figure 1 shows a summary of the 15 wind profiles used in this study, with the zonal and meridional components displayed respectively in the left and center columns, and the horizontal magnitudes in the right column. The vertical component is not estimated and is ignored throughout this study. The text label at right shows the date, campaign name, and Kp value for each group of wind profiles. The chronological ordering of the

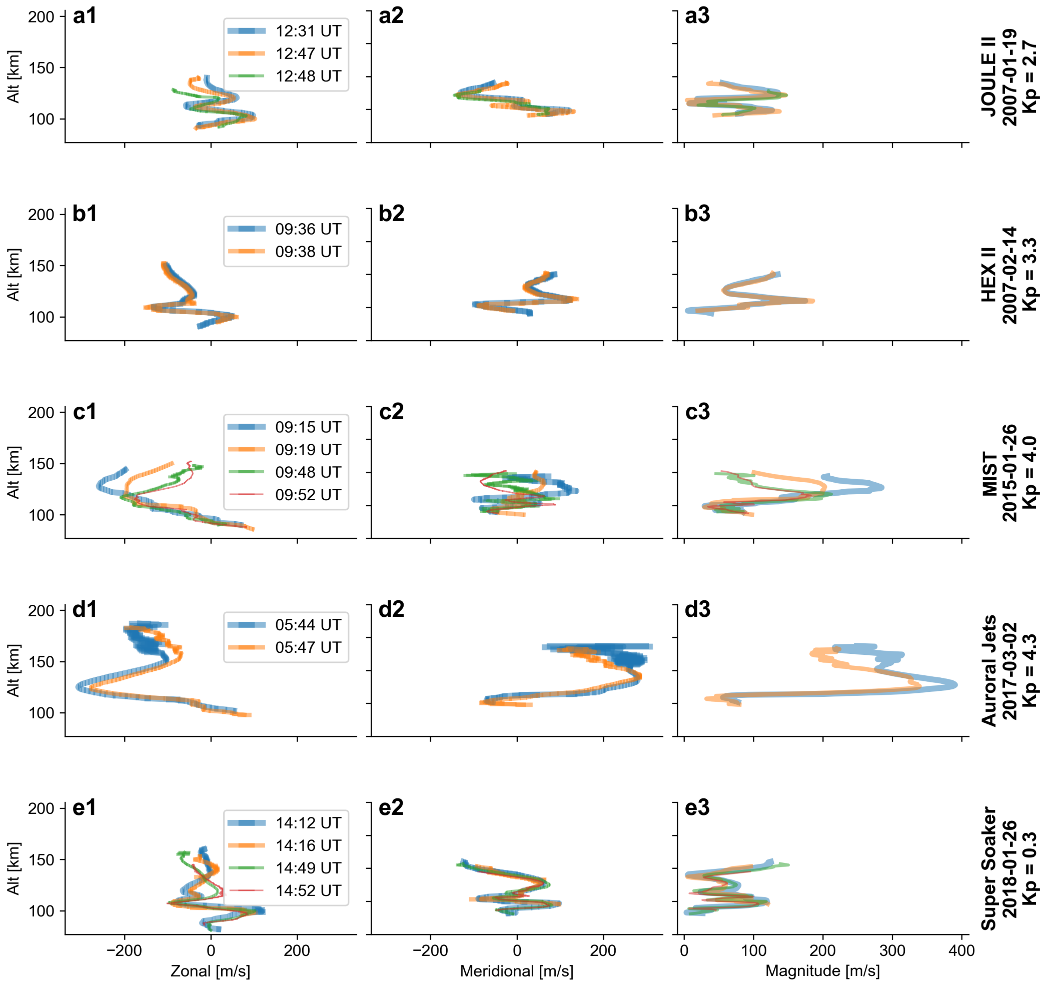

Figure 1. Summary of neutral wind profiles used in this study, given in the same order as the rocket campaigns in Table S1 in the Supporting Information. The zonal and meridional components are shown in the left and center columns, with the magnitude profiles shown in the right column. The campaign name and degree of geomagnetic activity are indicated in the caption at far right in each row.

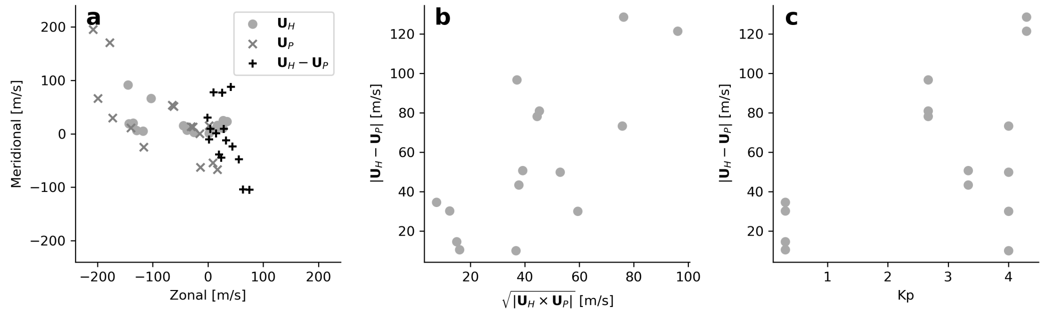

Figure 2. (a) Statistics of $\mathbf{U}_H$, $\mathbf{U}_P$, $\mathbf{U}_H - \mathbf{U}_P$. (b) The magnitude of the difference of $\mathbf{U}_H$ and $\mathbf{U}_P$ against the square root of the magnitude of their cross product. (c) The magnitude of the difference of $\mathbf{U}_H$ and $\mathbf{U}_P$ against Kp. This figure answers Question 1 posed at the beginning of Section 3 ("How large is the observed difference between $\mathbf{U}_H$ and $\mathbf{U}_P$?"), and gives an impression of the typical magnitudes of these quantities, which appear in Equations 10–12.

rows of Figure 1 coincidentally also orders the wind profiles by Kp, aside from the last row (Super Soaker campaign) for which Kp was lowest (Kp= 0.3). The magnitudes of the wind profiles show a clear tendency to increase with increasing Kp. Some details about each campaign, including the time of each measurement (center time of images used for triangulation) and the availability of PFISR measurements, are given in Table S1 of the Supporting Information.

For each wind profile shown in Figure 1 we calculate corresponding $\mathbf{U}_H$ and $\mathbf{U}_P$ vectors via Equation 9. This calculation in turn requires calculation of conductivity profiles, which we perform using Poker Flat Incoherent Scatter Radar (PFISR) measurements, the NRLMSIS®2.0 empirical atmospheric model (Emmert et al., 2020), and the International Reference Ionosphere (IRI) 2016 model (Bilitza et al., 2017), following the methodology of Ieda (2020). The steps of this process are summarized and illustrated in Text S3 and Figure S1 of the Supporting Information.

3.2 Statistics of $\mathbf{U}_H$ and $\mathbf{U}_P$

After performing the procedure described in the previous subsection for all 15 neutral wind profiles, we obtain the estimates of $\mathbf{U}_H$ and $\mathbf{U}_P$ as well as their difference ($\mathbf{U}_H - \mathbf{U}_P$) shown in Figure 2a. For these neutral wind profiles the zonal component of $\mathbf{U}_H$ and $\mathbf{U}_P$ exhibits a tendency to be negative (westward), while the meridional components exhibit a slight tendency to be positive (northward). The magnitudes of $\mathbf{U}_H$ and $\mathbf{U}_P$ are of order 10–100 m/s, with the magnitude of the former tending to be the smaller of the two. Given the magnitude of the geomagnetic field at PFRR (∼54,000 nT at 110-km altitude), these magnitudes correspond to electric field equivalents of ∼0.5–5 mV/m.

We do not attempt to draw general conclusions about $\mathbf{U}_H$ and $\mathbf{U}_P$ on the basis of the estimates shown in Figure 2a, as they are representative of only one location (PFRR) for a sparsely sampled range of universal times (∼06–14 UT) and one season (January to March), as indicated in Table S1 of the Supporting Information. It nevertheless seems probable that the range of magnitudes of $\mathbf{U}_H$ and $\mathbf{U}_P$ shown in Figure 2a is typical at high latitudes during low to moderate geomagnetic activity.

Figure 2b plots $|\mathbf{U}_H - \mathbf{U}_P|$ against the magnitude of their cross product. The magnitudes of these two quantities are relevant to examine as they both appear in Equations 10 and 12. From values in this panel we see that the typical magnitude of "mismatch" be-

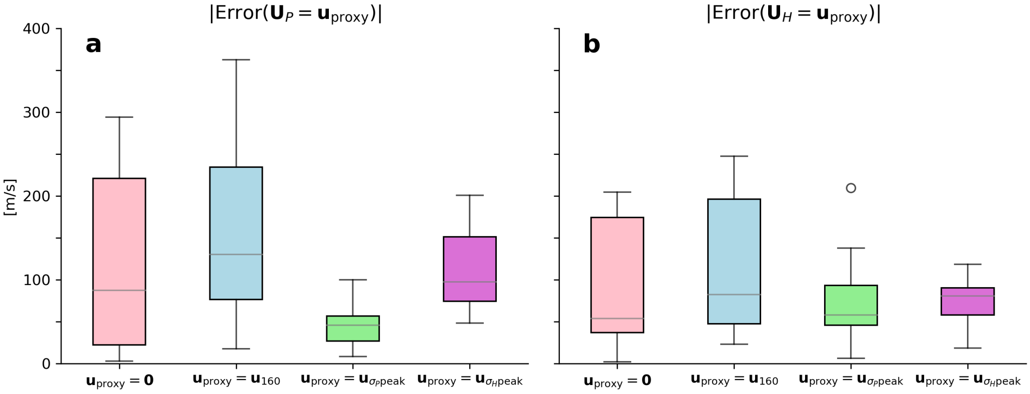

Figure 3. (a) For 15 neutral wind profiles, statistics of the magnitude of the Pedersen-weighted neutral wind ($\mathbf{U}_P$, pink), the magnitude of the differences between $\mathbf{U}_P$ and the neutral wind at 160-km altitude ($\mathbf{u}_{160}$, blue), the magnitude of the difference between $\mathbf{U}_P$ and the neutral wind at the height at which the Pedersen conductance maximizes ($\mathbf{u}_{\sigma_P\text{peak}}$, green), and the magnitude of the difference between $\mathbf{U}_P$ and the neutral wind at the height at which the Hall conductance maximizes ($\mathbf{u}_{\sigma_H\text{peak}}$, violet). The first and second represent the error associated with assuming $\mathbf{U}_P = 0$ m/s and $\mathbf{U}_P = \mathbf{u}_{160}$; the latter two represent the error associated with assuming $\mathbf{U}_P$ is one of the two proxies. The horizontal lines above and below each box plot are respectively given by $Q3 + 1.5\text{IQR}$ and $Q1 - 1.5\text{IQR}$ (see main text). (b) Same as panel a, but for the Hall-weighted neutral wind $\mathbf{U}_H$. The point of this figure is to answer Question 2 posed at the beginning of Section 3 by assessing whether any proxy for the Hall- and Pedersen-weighted neutral winds statistically incurs less error than simply assuming that they are zero.

tween $\mathbf{U}_H$ and $\mathbf{U}_P$ is ~5–130 m/s. It is also evident that the quantities $|\mathbf{U}_H - \mathbf{U}_P|$ and $|\mathbf{U}_H \times \mathbf{U}_P|$ are positively correlated.

Figure 2c plots $|\mathbf{U}_H - \mathbf{U}_P|$ against the Kp value during each rocket launch, with the former tending to be smallest for low Kp and the degree of scatter increasing for increasing Kp.

3.3 Proxies for the Hall- and Pedersen-weighted neutral winds

Here we address Question 2 posed at the beginning of this section: How much better are various rule-of-thumb approximations for the neutral wind than simply assuming $\mathbf{U}_H = \mathbf{U}_P = \mathbf{u} = 0$? To answer this question, Figure 3a shows the error distribution $\text{Error}\left(\mathbf{U}_P = \mathbf{u}_{\text{proxy}}\right) = |\mathbf{U}_P - \mathbf{u}_{\text{proxy}}|$ associated with the assumption $\mathbf{U}_P = \mathbf{u}_{\text{proxy}}$, where $\mathbf{u}_{\text{proxy}}$ is taken to be one of $\mathbf{0}$, $\mathbf{u}_{160}$, $\mathbf{u}_{\sigma_P\text{peak}}$, or $\mathbf{u}_{\sigma_H\text{peak}}$. These are respectively the zero vector, the neutral wind at 160-km altitude, the neutral wind at the altitude where the Pedersen conductivity profile peaks, and the neutral wind at the altitude where the Hall conductivity profile peaks. Each distribution is presented as a vertical box plot, where each box indicates (from top to bottom) the upper quartile $Q3$, the median, and lower quartile $Q1$. The horizontal lines above and below are respectively given by $Q3 + 1.5\text{IQR}$ and $Q1 - 1.5\text{IQR}$, where $\text{IQR} = Q3 - Q1$ is the interquartile range. In analogy with Figure 3a, Figure 3b shows the error associated with assuming $\mathbf{U}_H = \mathbf{u}_{\text{proxy}}$.

Figure 3a demonstrates that for the 15 neutral wind profiles examined in this study, assuming $\mathbf{U}_P = \mathbf{u}_{\sigma_P\text{peak}}$ statistically incurs less error than assuming $\mathbf{U}_P = \mathbf{0}$, $\mathbf{U}_P =$

$\mathbf{u}_{160}$, or $\mathbf{U}_P = \mathbf{u}_{\sigma_H \mathrm{peak}}$. For $\mathbf{U}_H$, Figure 3b shows that assuming $\mathbf{U}_H = \mathbf{0}$ incurs the least median error of any proxy, although the overall range of errors is smallest for $\mathbf{U}_H = \mathbf{u}_{\sigma_H \mathrm{peak}}$.

In the simulations that Lu et al. (1995) presented, they found that the "effective neutral wind pattern" (what we term the Pedersen-weighted neutral wind $\mathbf{U}_P$) is equivalent to the neutral wind pattern at 160-km altitude. This rule of thumb has been employed by Baker et al. (2004) and Billett et al. (2018). Figure 3a shows that for the majority of the 15 neutral wind profiles examined in this study, this rule of thumb yields a larger error than the more naïve assumption that $\mathbf{u} = \mathbf{0}$.

4 Discussion

Lu et al. (1995), Baker et al. (2004), and Billett et al. (2018) all make use of the idea of a two-dimensional "effective neutral wind" pattern. As we have shown in Section 2, the most suitable definition for the "effective neutral wind" in terms of smallest error incurred is what we have termed the Pedersen-weighted neutral wind $\mathbf{U}_P$ given in Equation 9. Based on Lu et al. (1995), the latter two pick up on the idea of the neutral winds at 160-km altitude as being the "effective" altitude.

Regarding Question 3 posed at the beginning of Section 3—whether the observed differences between $\mathbf{U}_H$ and $\mathbf{U}_P$ are meaningful for assessments of IT electrodynamics—we get some idea of the importance of the distinction between them by examining the magnitude of the quantity $B\mathbf{B}\cdot(\mathbf{U}_H \times \mathbf{U}_P)$ in the expression for M given by Equation 11. This quantity appears in the expressions 13 and 14 for height-integrated conductances when the distinction between $\mathbf{U}_H$ and $\mathbf{U}_P$ is maintained. From Figure 2, we have $|\mathbf{U}_H \times \mathbf{U}_P| \sim \mathcal{O}(10^2\text{–}10^4)$ (m/s)^2 such that $\sqrt{|B\mathbf{B} \cdot (\mathbf{U}_H \times \mathbf{U}_P)\,|} \sim \mathcal{O}(0.5\text{–}5)$ mV/m. This makes clear that ignoring the distinction between $\mathbf{U}_H$ and $\mathbf{U}_P$ can incur a non-negligible error in estimation of Σ_H and Σ_P, even when the "effective neutral wind" $\mathbf{U}_P$ is used in Equations 5–6 for height-integrated conductance. With the present severe lack of systematic measurements of the neutral wind, this result underscores the difficult situation facing studies such as those of Weimer and Edwards (2021) and Hatch et al. (2023), in which the authors attempt to estimate Σ_H and Σ_P on the basis of Equations 5–6 assuming $\mathbf{u} = 0$: in a number of scenarios where one wishes to represent high-latitude IT electrodynamics in two dimensions, one misses potentially important aspects of this coupling by representing the neutral wind with a single variable.

In the context of Question 3 it is also relevant to compare the neutral wind term $\Sigma_P|\mathbf{U}_P\times\mathbf{B}|^2$ with the explicitly height-integrated term $\int \sigma_P|\mathbf{u}\times\mathbf{B}|^2 dh$ in Equation 15, as discussed in Section 2. Figure 4 shows that the former underestimates the latter by 9–96%, with the magnitude of underestimation decreasing as $\int \sigma_P|\mathbf{u}\times\mathbf{B}|^2 dh$ increases, and the gap between $\Sigma_P|\mathbf{U}_P\times\mathbf{B}|^2$ and $\int \sigma_p|\mathbf{u}\mathbf{B}|^2 dh$ tending to decrease with increasing Kp.

The results in Section 2 have some bearing on the "key MI coupling equation" derived from current continuity that is mentioned in the introduction,

$$\nabla \cdot \mathbf{J}_\perp = -j_\parallel, \tag{17}$$

where the integrated perpendicular current $\mathbf{J}_\perp$ is given by a height- or field line-integrated form of Ohm's law (i.e., $\mathbf{J}_\perp = \bar{\bar{\Sigma}}\cdot[\mathbf{E}_\perp + \mathbf{U} \times \mathbf{B}]$) in terms of the potential electric field $\mathbf{E}_\perp = -\nabla_\perp \Phi$ and the ionospheric conductance tensor $\bar{\bar{\Sigma}}$. The development in Section 2 shows that it is strictly speaking not possible to formulate the height-integrated ionospheric Ohm's law as given by Equation 7 in terms of the conductance tensor $\bar{\bar{\Sigma}}$, because $\mathbf{F}_H$ and $\mathbf{F}_P$ are generally not identical. It is unclear from the results presented in Figure 3 how much the differences between $\mathbf{U}_H$ and $\mathbf{U}_P$ can affect the description of IT electrodynamics in models that employ some form of this equation. What is true statisti-

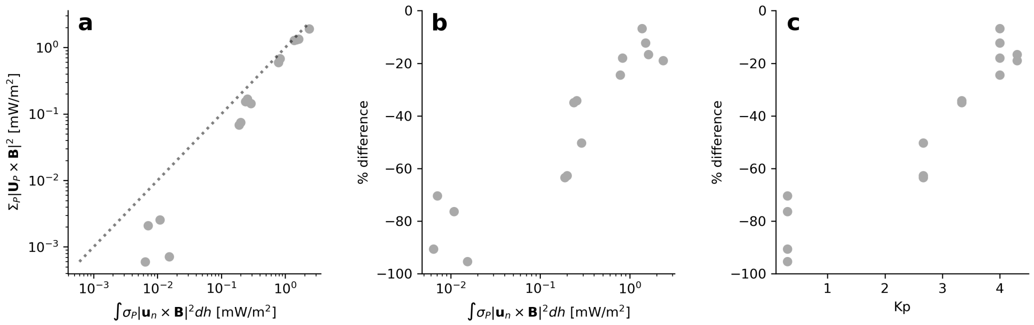

Figure 4. (a) Comparison of the difference between the height-integrated neutral wind term $\int \sigma_P |\mathbf{u} \times \mathbf{B}|^2 dh$ (last term on RHS of Equation 15) and the lower-bound approximation $\Sigma_P |\mathbf{U}_P \times \mathbf{B}|^2$. (b) Percent difference between these quantities relative to $\int \sigma_P |\mathbf{u} \times \mathbf{B}|^2 dh$. (c) Percent difference as a function of Kp. The point of this figure is to assess how much the lower-bound approximation underestimates the magnitude of the integral $\int \sigma_P |\mathbf{u} \times \mathbf{B}|^2 dh$.

cally is that the magnitude of the difference between the Hall-weighted and Pedersen-weighted neutral wind terms tends to increase with increasing geomagnetic activity (Figure 2c), where in this study the latter is measured by the Kp index.

Regarding MI coupling in global models, it is relevant to observe that Equation 17 is not the state of the art: ionosphere-thermosphere models such as the Whole Atmosphere Community Climate Model With Thermosphere and Ionosphere Extension (WACCM-X, Liu et al., 2018) and the Thermosphere-Ionosphere-Electrodynamics General Circulation Model (Qian et al., 2014) use the 2D continuity equation given in the more advanced treatment of Richmond (1995). The Richmond (1995) equation generalizes Equation 17 and does, in fact, take stock of the three-dimensional nature of the neutral wind field.

In one sense this study is only one more voice in the chorus of recent literature calling for additional neutral wind measurements (Sarris, 2019; Heelis & Maute, 2020; Palmroth et al., 2021; Dhadly et al., 2023). On the other hand, this study points out a fundamental limitation of 2D descriptions of IT electrodynamics: Even when an appropriately defined neutral wind term is used (the Pedersen-weighted neutral wind), any estimate of height-integrated Joule heating on the basis of height-integrated and averaged quantities is mathematically guaranteed to be a lower bound of the actual height-integrated Joule heating, with some tendency for the pure neutral wind term to be less strongly underestimated with increasing Kp.

Regarding our finding in Section 3.3 and Figure 3 that the assumption $\mathbf{u} = 0$ is statistically a better estimate for both $\mathbf{U}_H$ and $\mathbf{U}_P$ than the neutral winds at 160-km altitude, $\mathbf{u}_{160}$, this study deals with a limited selection of neutral wind profiles at one geographical location and over a limited range of altitudes. The lack of statistics precludes drawing general conclusions. Our results do nevertheless indicate that one should be skeptical of "quick fixes" for the neutral wind problem, such as ignoring the winds or representing them with proxies. Figure 3 also suggests that the assumption $\mathbf{U}_H = \mathbf{U}_P = \mathbf{u}_{\sigma_P,\mathrm{peak}}$ is likely an improvement over simply assuming $\mathbf{U}_H = \mathbf{U}_P = \mathbf{u} = 0$. This points to the utility of techniques and measurements involving, for example, Doppler spectroscopy which in some conditions enable estimation of the neutral wind profiles over limited ranges of altitudes between 120 and 200 km where the Pedersen conductivity profile may peak (Branning et al., 2022; Dhadly et al., 2023).

Open Research Section

The NRLMSIS®2.0, IRI 2016, and IGRF-13 models are respectively queried via the `nrlmsis2.0` (Hirsch, 2020), `iri2016` (Hirsch, 2018), and `ppigrf` (Laundal, 2023) Python packages. Scripts and data used to make the plots shown in this study are available at Zenodo (Hatch & Mesquita, 2024).

Acknowledgments

This study is supported as part of Swarm Data, Innovation, and Science Cluster (DISC) activities, and is funded by ESA contract no. 4000109587/13/I-NB. SMH and KML were also supported by the Trond Mohn Research Foundation. SMH was additionally supported by the Research Council of Norway, contract 344061. KML was additionally supported by the European Union (ERC, DynaMIT, 101086985), and the Research Council of Norway, contract 300844/F50. JKB was supported with funding from Canadian Space Agency grant 15SUSWARM. HV is supported by the Academy of Finland project 354521. RM was supported with funding from NASA Grant with contract number 80NSSC23K0094. The authors thank A. Bhatt (SRI) for helpful guidance regarding the use of PFISR data.

References

Amm, O. (2001, nov). The elementary current method for calculating ionospheric current systems from multisatellite and ground magnetometer data. *Journal of Geophysical Research: Space Physics*, *106*(A11), 24843–24855. Retrieved from `https://doi.org/10.1029/2001JA900021http://doi.wiley.com/10.1029/2001JA900021` doi: 10.1029/2001JA900021

Baker, J. B. H., Zhang, Y., Greenwald, R. A., Paxton, L. J., & Morrison, D. (2004, may). Height-integrated Joule and auroral particle heating in the night side high latitude thermosphere. *Geophysical Research Letters*, *31*(9). Retrieved from `http://doi.wiley.com/10.1029/2004GL019535` doi: 10.1029/2004GL019535

Bilitza, D., Altadill, D., Truhlik, V., Shubin, V., Galkin, I., Reinisch, B., & Huang, X. (2017, 2). International reference ionosphere 2016: From ionospheric climate to real-time weather predictions. *Space Weather*, *15*, 418-429. doi: 10.1002/2016SW001593

Billett, D. D., Grocott, A., Wild, J. A., Walach, M.-T., & Kosch, M. J. (2018, mar). Diurnal Variations in Global Joule Heating Morphology and Magnitude Due To Neutral Winds. *Journal of Geophysical Research: Space Physics*, *123*, 2398– 2411. Retrieved from `http://doi.wiley.com/10.1002/2017JA025141` doi: 10.1002/2017JA025141

Branning, K., Conde, M., Larsen, M., & Troyer, R. (2022, 5). Resolving vertical variations of horizontal neutral winds in earth's high latitude space-atmosphere interaction region (sair). *Journal of Geophysical Research: Space Physics*, *127*. doi: 10.1029/2021JA029805

Burchill, J. K., Clemmons, J. H., Knudsen, D. J., Larsen, M., Nicolls, M. J., Pfaff, R. F., ... Sangalli, L. (2012, 2). High-latitude e region ionosphere-thermosphere coupling: A comparative study using in situ and incoherent scatter radar observations. *Journal of Geophysical Research: Space Physics*, *117*. doi: 10.1029/2011JA017175

Chapman, S. (1956, aug). The electrical conductivity of the ionosphere: A review. *Il Nuovo Cimento*, *4*(S4), 1385–1412. Retrieved from `http://link.springer.com/10.1007/BF02746310` doi: 10.1007/BF02746310

Cole, K. (1975, jun). Energy deposition in the thermosphere caused by the solar wind. *Journal of Atmospheric and Terrestrial Physics*, *37*(6-7), 939–949. Retrieved from `https://linkinghub.elsevier.com/retrieve/pii/0021916975900082` doi: 10.1016/0021-9169(75)90008-2

Dhadly, M., Sassi, F., Emmert, J., Drob, D., Conde, M., Wu, Q., ... Nicholas, A. (2023, 1). Neutral winds from mesosphere to thermosphere—past, present, and future outlook. *Frontiers in Astronomy and Space Sciences*, *9*. doi: 10.3389/fspas.2022.1050586

Emmert, J. T., Drob, D. P., Picone, J. M., Siskind, D. E., Jones, M., Mlynczak, M. G., ... Yuan, T. (2020, sep). NRLMSIS 2.0: A whole-atmosphere empirical model of temperature and neutral species densities. *Earth and Space Science*. Retrieved from `https://onlinelibrary.wiley.com/doi/10.1029/2020EA001321` doi: 10.1029/2020EA001321

Farley, D. T. (1959, 9). A theory of electrostatic fields in a horizontally stratified ionosphere subject to a vertical magnetic field. *Journal of Geophysical Research*, *64*, 1225-1233. Retrieved from `http://doi.wiley.com/10.1029/JZ064i009p01225` doi: 10.1029/JZ064i009p01225

Green, D. L., Waters, C. L., Korth, H., Anderson, B. J., Ridley, A. J., & Barnes, R. J. (2007, may). Technique: Large-scale ionospheric conductance estimated from combined satellite and ground-based electromagnetic data. *Journal of Geophysical Research: Space Physics*, *112*(A5). Retrieved from `http://doi.wiley.com/10.1029/2006JA012069` doi: 10.1029/2006JA012069

Hatch, S. M., & Mesquita, R. L. A. (2024, April). *Resource for Hatch et al (2024), "What is the neutral wind in height-integrated electrodynamics?".* Zenodo. Retrieved from `https://doi.org/10.5281/zenodo.11091983` doi: 10.5281/zenodo.11091983

Hatch, S. M., Vanhamäki, H., Laundal, K. M., Reistad, J. P., Burchill, J., Lomidze, L., ... Tesfaw, H. (2023). Does high-latitude ionospheric electrodynamics exhibit hemispheric mirror symmetry? *EGUsphere*, *2023*, 1–41. Retrieved from `https://egusphere.copernicus.org/preprints/2023/egusphere-2023-2920/` doi: 10.5194/egusphere-2023-2920

Heelis, R., & Maute, A. (2020, 2). Challenges to understanding the earth's ionosphere and thermosphere. *Journal of Geophysical Research: Space Physics*. Retrieved from `https://onlinelibrary.wiley.com/doi/abs/10.1029/2019JA027497` doi: 10.1029/2019JA027497

Heppner, J. P., & Miller, M. L. (1982, mar). Thermospheric winds at high latitudes from chemical release observations. *Journal of Geophysical Research: Space Physics*, *87*(A3), 1633–1647. Retrieved from `http://doi.wiley.com/10.1029/JA087iA03p01633` doi: 10.1029/JA087iA03p01633

Hirsch, M. (2018). *iri2016.* https://doi.org/10.5281/zenodo.240895. doi: 10.5281/zenodo.240895

Hirsch, M. (2020). *nrlmsis2.0.* https://github.com/space-physics/nrlmsis2.0.

Ieda, A. (2020, feb). Ion-Neutral Collision Frequencies for Calculating Ionospheric Conductivity. *Journal of Geophysical Research: Space Physics*, *125*(2). Retrieved from `https://onlinelibrary.wiley.com/doi/10.1029/2019JA027128` doi: 10.1029/2019JA027128

Larsen, M. F. (2002, aug). Winds and shears in the mesosphere and lower thermosphere: Results from four decades of chemical release wind measurements. *Journal of Geophysical Research: Space Physics*, *107*(A8), SIA 28–1–SIA 28–14. Retrieved from `http://doi.wiley.com/10.1029/2001JA000218` doi: 10.1029/2001JA000218

Laundal, K. M. (2023). *Pure python international geomagnetic reference field (ppigrf).* Retrieved from `https://github.com/klaundal/ppigrf` doi: 10.5281/zenodo.5962660

Laundal, K. M., Reistad, J. P., Hatch, S. M., Madelaire, M., Walker, S., Hovland, A. Ø., ... Sorathia, K. A. (2022, may). Local Mapping of Polar Ionospheric Electrodynamics. *Journal of Geophysical Research: Space Physics*, *127*(5). Retrieved from `https://onlinelibrary.wiley.com/doi/10.1029/2022JA030356` doi: 10.1029/2022JA030356

Liu, H., Bardeen, C. G., Foster, B. T., Lauritzen, P., Liu, J., Lu, G., ... Wang, W. (2018, 2). Development and validation of the whole atmosphere community climate model with thermosphere and ionosphere extension (waccm-x 2.0). *Journal of Advances in Modeling Earth Systems*, *10*, 381-402. doi: 10.1002/2017MS001232

Lu, G., Richmond, A. D., Emery, B. A., & Roble, R. G. (1995, oct). Magnetosphere-ionosphere-thermosphere coupling: Effect of neutral winds on energy transfer and field-aligned current. *Journal of Geophysical Research: Space Physics*, *100*(A10), 19643–19659. Retrieved from http://dx.doi.org/10.1029/95JA00766http://doi.wiley.com/10.1029/95JA00766 doi: 10.1029/95JA00766

Mannucci, A. J., McGranaghan, R., Meng, X., & Verkhoglyadova, O. P. (2022, nov). An Analysis of Magnetosphere-Ionosphere Coupling That Is Independent of Inertial Reference Frame. *Journal of Geophysical Research: Space Physics*, *127*(11). Retrieved from https://onlinelibrary.wiley.com/doi/10.1029/2021JA030009 doi: 10.1029/2021JA030009

Matsuo, T. (2020). Recent progress on inverse and data assimilation procedure for high-latitude ionospheric electrodynamics. In (p. 219-232). Springer International Publishing. Retrieved from http://link.springer.com/10.1007/978-3-030-26732-2_10 doi: 10.1007/978-3-030-26732-2_10

Merkin, V. G., & Lyon, J. G. (2010, oct). Effects of the low-latitude ionospheric boundary condition on the global magnetosphere. *Journal of Geophysical Research: Space Physics*, *115*(A10). Retrieved from http://doi.wiley.com/10.1029/2010JA015461 doi: 10.1029/2010JA015461

Mesquita, R. L. A. (2021). *An Observational Investigation of Mid-Latitude Thermospheric Temperatures and High-Latitude E-Region Neutral Wind Structures* (Dissertation, Clemson University). Retrieved from https://tigerprints.clemson.edu/all_dissertations/2802/

Mukhopadhyay, A., Jia, X., Welling, D. T., & Liemohn, M. W. (2021, 4). Global magnetohydrodynamic simulations: Performance quantification of magnetopause distances and convection potential predictions. *Frontiers in Astronomy and Space Sciences*, *8*. doi: 10.3389/fspas.2021.637197

Palmroth, M., Grandin, M., Sarris, T., Doornbos, E., Tourgaidis, S., Aikio, A., ... Yamauchi, M. (2021, 2). Lower-thermosphere–ionosphere (lti) quantities: current status of measuring techniques and models. *Annales Geophysicae*, *39*, 189-237. Retrieved from https://angeo.copernicus.org/articles/39/189/2021/ doi: 10.5194/angeo-39-189-2021

Parker, E. N. (2007). *Conversations on Electric and Magnetic Fields in the Cosmos*. Princeton University Press. Retrieved from https://www.jstor.org/stable/10.2307/j.ctt2111gdt doi: 10.2307/j.ctt2111gdt

Qian, L., Burns, A. G., Emery, B. A., Foster, B., Lu, G., Maute, A., ... Wang, W. (2014, 3). The ncar tie-gcm. In (p. 73-83). John Wiley & Sons, Ltd. Retrieved from https://onlinelibrary.wiley.com/doi/10.1002/9781118704417.ch7http://dx.doi.org/10.1002/9781118704417.ch7 doi: 10.1002/9781118704417.ch7

Richmond, A. D. (1995). Ionospheric Electrodynamics Using Magnetic Apex Coordinates. *Journal of geomagnetism and geoelectricity*, *47*(2), 191–212. doi: 10.5636/jgg.47.191

Richmond, A. D., & Kamide, Y. (1988). Mapping electrodynamic features of the high-latitude ionosphere from localized observations - Technique. *Journal of Geophysical Research*, *93*(A6), 5741–5759. doi: 10.1029/JA093iA06p05741

Sangalli, L., Knudsen, D. J., Larsen, M. F., Zhan, T., Pfaff, R. F., & Rowland, D. (2009, apr). Rocket-based measurements of ion velocity, neutral wind, and electric field in the collisional transition region of the auroral ionosphere. *Journal of Geophysical Research: Space Physics*, *114*(A4).

Retrieved from http://doi.wiley.com/10.1029/2008JA013757 doi: 10.1029/2008JA013757
Sarris, T. E. (2019, 7). Understanding the ionosphere thermosphere response to solar and magnetospheric drivers: status, challenges and open issues. *Philosophical Transactions of the Royal Society A: Mathematical, Physical and Engineering Sciences*, *377*, 20180101. Retrieved from https://royalsocietypublishing.org/doi/10.1098/rsta.2018.0101 doi: 10.1098/rsta.2018.0101
Weimer, D., & Edwards, T. (2021, jan). Testing the electrodynamic method to derive height-integrated ionospheric conductances. *Annales Geophysicae*, *39*(1), 31–51. Retrieved from https://angeo.copernicus.org/articles/39/31/2021/ doi: 10.5194/angeo-39-31-2021